ARCHIVES
of
FOUNDRY ENGINEERING

ISSN (2299-2944)
Volume 2025
Issue 2/2025

157 – 172

18/2

10.24425/afe.2025.153806

Published quarterly as the organ of the Foundry Commission of the Polish Academy of Sciences

Investigation on Low Stress Scratching Abrasion Resistance Influencing Residual Stress in Nickel Chromium Alloyed Iron

Sandeep Mashetty A. [a] *, Sampathkumaran P.[b], Ranjitha P. [c], Chithirai Pon Selvan [d], Shridhar Deshpande C. [e], Avinash Lakshmikanthan [f], Manjunath Patel G.C. [g, *]

[a] Department of Mechanical Engineering, LingarajAppa Engineering College, Bidar, Affiliated to VTU, Belagavi, Karnataka 585403, India
[b] Département of Mechanical Engineering, Sambhram Institute of Technology, Bangalore Affiliated to VTU, Belagavi, Karnataka, India
[c] Department of Mechanical Engineering, Dayananda Sagar College of Engineering, Bangalore Affiliated to VTU, Belagavi, Bangalore, Karnataka 560078, India
[d] School of Science and Engineering, Curtin University, Dubai, 345031, United Arab Emirates
[e] Department of Mechanical Engineering, Sri Venkateshwara College of Engineering, Bengaluru Affiliated to VTU, Belagavi, Karnataka, India
[f] Department of Mechanical Engineering, Nitte Meenakshi Institute of Technology, Bengaluru, Karnataka, India
[g] PES Institute of Technology and Management, Shivamogga. Visvesvaraya Technological University, Belagavi, India
* Corresponding author: E-mail address: manju09mpm05@gmail.com
* Corresponding author: E-mail address: shmashetty@gmail.com

Received 08.12.2024; accepted in revised form 10.03.2025; available online 30.06.2025

Abstract

In thermal power plants, advanced wear-resistant alloyed irons have been used for over three decades to enhance the longevity of parts. Ni-hard irons, high chromium irons, and HCHC materials are commonly used in components like liners, bull rig segments, and orifices. These components are exposed to various types of failures, including abrasion, erosion, corrosion, and fatigue. Nickel-chromium irons, particularly Ni-hard 4 and high chromium irons, have proven effective in extending component life. However, the impact of scratching abrasion resistance on residual stress (RS) buildup has been less studied. This research investigates the wear behavior of nickel-chromium irons, focusing on Ni-hard and high chromium-manganese iron. Abrasion loss was measured using a rubber wheel abrader according to ASTM standards, and RS was evaluated through X-ray diffraction before and after abrasion testing. Supporting analyses, including hardness testing, phase analysis, carbide morphology, and microstructural evaluations, were performed to correlate abrasion with RS data. Scanning electron microscopy (SEM) was used to assess wear phenomena. The HiCr sample displays the highest hardness and compression strength, and lowest abrasion loss, followed by NH4, HiCr5Mn, HiCr10Mn, and HiCr15Mn samples. Higher Mn content introduces more brittle characteristics into the fracture process. Among HiCrMn samples, HiCr5Mn is preferred for abrasion resistance application; on the other hand, HiCr15Mn may be suitable in the field, possessing better resistance to impact and load bearing applications.

Keywords: Wear resistance, Nickel-chromium irons, Residual stress, Abrasion

1. Introduction

Nickel-chromium iron alloy is a promising wear-resistant material that gained prominence in engineering applications due to its excellent tribe-corrosion properties and thermal stability [1, 2]. Material flexibility allows various processing techniques, and its properties can be altered to meet specific functional requirements [3, 4, 5]. Nickel-chromium iron alloy offers high temperature and corrosive resistance, ensures best suited for critical applications [6]. Advances in metallurgical engineering also allowed the refining of microstructure in nickel-chromium alloys such that their abrasion resistance can be enhanced [7]. Revolutions in material research allow industry personnel to enhance material efficiency and reliability. Nickel-chromium alloyed iron components used in automotive and aerospace components undergo abrasion resistance [8, 9]. Scratch abrasion resistance is a critical property influenced by material composition, microstructure, and residual stress [10]. Understanding the interplay of influencing parameters is important for optimizing material performance and durability.

Residual stress (RS) occurs during casting, welding, and heat treatment processes that significantly impact the material behavior [11]. The mechanical properties, such as hardness, fatigue resistance, wear/abrasion resistance, and structural features, influence the RS levels in any material [12]. Compressive residual stress is known to improve wear resistance and suppress crack propagation, thereby enhancing the material's service life. On the other hand, tensile residual stresses can serve as stress concentrators under operational loads by increasing the susceptibility to failure. With proper knowledge of such contrasting states of stress within specific material systems, like nickel-chromium alloyed iron, performance optimization in abrasive environments should be possible. Nevertheless, the relationship between residual stress and abrasion resistance in nickel-chromium alloyed iron has not yet explored the material behavior.

The above literature review draws significant attention from researchers across the globe focused on studying recent materials and their relationship with residual stress and abrasion resistance that could widen engineering applications. The influence of residual stress exerted on fatigue behavior in metallic alloys emphasized the complete characterization and mitigation strategies [13]. The microstructural defects and grain boundaries influencing abrasive wear are explained with fundamental material wear behavior mechanisms [14]. The residual stress in high-strength steel emphasizes the correlation between wear properties and compressive stress that could improve resistance against crack initiation [15]. Better abrasion resistance in enhancing the overall mechanical properties was emphasized by examining the carbide precipitation in nickel-chromium alloys [16]. The interrelation between thermal stresses and microstructural evolution in high-chromium iron alloys and the need for accurate control of processing conditions were explained [17]. The impact of heat treatment in enhancing the morphology of carbides and the wear resistance in high-chromium white cast iron was highlighted [18]. Their research work explained the impact of thermal processing on microstructural properties. The residual stresses developed during the laser cladding process enhance the wear resistance of nickel-based alloy coatings, highlighting the importance of advanced surface engineering techniques [19]. The influence of shot peening technique on abrasive wear, where the compressive residual stresses resulted in significant inhibition of crack initiation under abrasive abrasion conditions [20]. The relationship between composition and processing conditions is correlated with material performance, microstructural evolution, and mechanical properties of nickel-chromium alloys [21, 22]. The above literature review sets the background to define aim and methodologies by defining gaps in research that relate abrasion with residual stress in HiCr alloys.

The present work addresses the gaps by highlighting insights into the residual stress relationship with scratch abrasion resistance for different industrial-grade nickel-chromium iron alloyed materials. Integrating experimental analysis with theoretical frameworks could help investigators explore the impact of interaction effects by addressing the residual stress and material behavior subjected to abrasive conditions that determine the critical thresholds affecting the material performance. In addition, the investigation also examines how residual stress influences crack initiation and propagation, providing insights into failure mechanisms and guiding the optimization of material properties. Advanced characterization techniques such as X-ray diffraction (XRD), scanning electron microscopy (SEM), and hardness testing were applied to control the abrasion tests and microstructural analysis that detect phase transformations, carbide distributions, and surface or subsurface alterations. Correlating these factors with residual stress profiles and abrasion resistance will offer a holistic understanding of material behavior, paving the way for predictive models and next-generation wear-resistant materials. Combining advanced analytical techniques with rigorous abrasion testing reveals the mechanisms governing RS evolution during wear, enhancing material durability and reliability in demanding industrial applications like mining, automotive, and heavy machinery. The above results help investigators in decision-making that optimizes wear-resistant materials and sets benchmarks for designing alloys capable of withstanding extreme operational and load bearing (grinding media, liners, and impellers in thermal power plants) environments. Addressing both the microscopic and macroscopic aspects of material behavior enables investigators to make significant contributions to materials engineering and industrial design.

2. Experimental Procedure

Materials

The materials considered for the assessment of erosion damage affecting residual stresses are Ni-Hard 4 Iron and High chromium iron of Commercial grades (Figure 11), which have been considered for this study. HiCr and HiCrMn castings were produced by induction melting technique in a metal mould having dimensions of 150×150×10 mm^3 for cross-comparison. Mild steel in cold-rolled conditions has been identified in this study. The addition of Mn elements to Cr serves as an austenite stabilizing agent tends to withstand material subjected to load for applications in grinding media, liners, and impellers in thermal power plants [23].

Methods

The castings were prepared by the melting method using a

coreless type induction furnace of 15 kW, capacity operated at 9.6 kHz. The test samples (cavity dimensions: 150 X 150 X 10 mm^3) were produced in a grey cast iron metal mould is presented in Figure 1. An acetylene flame was used to heat the inner surfaces of the metal mould to remove the casting from the mould. The use of metal would have the distinct advantages of a good surface finish, less environmental pollution, and good dimensional stability. The casted cut section of samples (75 x 25 x 5 mm^3) prepared by cutting and grinding operations to conduct various tests is presented in Figure 2.

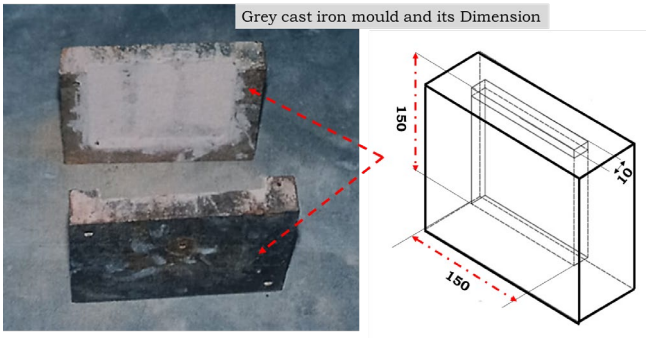

Fig. 1. Dimensions in mm of metal mould casting

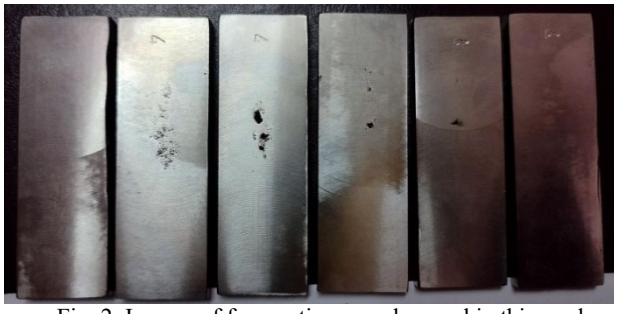
Fig. 2. Images of few casting samples used in this work

Heat Treatment

The Nickel chromium iron samples have been heat treated as per the details ºC [24, 25] given below.

(a) The Ni hard 4 was subjected to destabilization treatment at 820 ºC for 4 hours, followed by air cooling, and subsequently, subcritical treatment was given at 350 ºC.

(b) High chromium iron samples are austenite at 950 ºC, soaked for 6 hours, then quenched in oil followed by tempering treatment at 200 ºC for about half an hour and subsequently air cooled.

(c) High chromium manganese iron samples are austenite at 950 ºC, soaked for 6 hours, then quenched in oil, followed by tempering treatment at 200 ºC for about half an hour and then air cooled.

Optical emission Spectrophotometer

The chemical compositions have been determined using an optical emission spectrophotometer. The light generated by discharges is split by a diffraction grating to extract the emission spectra, enabling the determination of the chemical composition of the material under study. In this method, an electrical spark vaporizes a small portion of the material, creating plasma. The plasma emits light because the atoms and ions in it get excited. Each element in the sample emits light at a unique wavelength, which is characteristic of that element. The diffraction grating spreads the light into different wavelengths; the detector takes readings from the intensity. Intensity indicates how much each element was present in that sample. This method, particularly suitable for analyzing alloys like Ni-hard and HiCr, identifies other crucial elements like chromium, manganese, and carbon that define the strength, hardness, and resistance to wear properties of such materials. OES gives a clear and accurate result, which makes it indispensable to know the alloy compositions in this work.

Hardness

Hardness testing has been conducted on the samples using a Rockwell hardness C tester with a diamond cone indenter at a load of 150 kg. The tests are conducted according to the ASTM E18-07 standards. The Rockwell hardness test is one of the widely used methods for evaluating the surface hardness of materials. The test works on the principle of pressing a diamond cone indenter into the surface of the sample under a specified load. Then, the depth of the indentation and the hardness value is measured.

The use of the diamond cone indenter ensures the right results for hard materials, such as Ni-hard and HiCr alloys. Since all tests are run under ASTM standards, they are both uniform and reliable, and studies conducted earlier can be compared. Such hardness information plays a fundamental role in illustrating the mechanical performance and the wear resistance properties of tested alloys, with harder alloys, in most cases, giving better surface deformation resistance and wear properties.

Impact Energy

Drop weight Impact testing has been conducted on the samples using a (IT - 40 (ASTM) make FHI Equipment, Chennai, Tamil Nadu, India.) tester. The tests (describes the dimensions and geometry of samples) are conducted according to ASTM E23 standards. The IT – 40 tester is set up with an appropriate drop weight and height to strike the specimen placed in a designated holder on the tester to achieve the desired impact energy. The impact energy data were collected after each test for further analysis.

Microstructure

The light micrographs of the samples have been examined using a metallurgical microscope at a magnification of 500x. The sample preparation for microstructure was done by polishing using SiC emery paper of grit sizes 200, 400, 600, and 800, followed by cloth polishing involving diamond paste, kerosene, etc. The sample is then etched using the nital solution (3% nitric acid and 97% ethanol).

The step-by-step polishing process ensures a smooth finish and reflective surface, mainly for microstructural analysis. This polishing removes surface imperfections and scratches carried out successively finer grit sizes, with the last cloth having diamond paste producing a true mirror finish for microscopic detail examination.

Etching with nital solution selectively attacks the different phases of the material to reveal its microstructure. It brings out

carbides, martensite, and austenite regions, which enables the identification of key features such as grain boundaries and phase distributions. This high magnification of the microstructure yields important information regarding the hardness, toughness, and wear resistance of the material.

X-Ray Diffraction

The main purpose of this test is to measure the residual stress and retained austenite of the cast samples under investigation. The residual stress measurements were done on the specimens using the XRD method (Rigaku X-Ray stress Analysis) according to the ASTM-E915 Standard [26]. The X-ray radiation is made to impinge on the target material and allow the scattering to take place during diffraction and satisfying the Brags law condition $n\lambda=2d\sin\theta$ where θ is the Brags angle, λ is the wavelength of the X-ray radiation, d is the internal planar spacing. The photograph of the Residual stress machine used is shown in Figure 3. More details may be referred from the literature [26].

This technique is essential to understand the internal stresses in the materials, as residual stress affects mechanical properties like fatigue resistance, wear performance, and dimensional stability. Measurement of retained austenite with XRD also assists in phase composition evaluation, which is a critical parameter determining hardness and ductility in the alloys under investigation.

The Rigaku X-Ray Stress Analysis system has high precision and reliability in terms of examination and is suitable for hard alloys such as Ni-hard and HiCr. With the use of ASTM standards, the results would be accurate and comparable to other studies, thus setting a solid foundation for the correlation of microstructural features with mechanical performance.

Fig. 3. X-ray Testing Machine

In this experiment, the tests were done for different Ψ angles (Ψ is the angle between plane normal and surface normal) 2θ plane shafts are measured and a plot $\Delta 2\theta$ vs $\Delta\sin^2\Psi$ is plotted. Depending on the nature and magnitude of the x ray intensity levels, the strain is measured as Δd, then the stress is calculated using equation 1 where in the slope $\left(\frac{\Delta 2\theta}{\Delta \sin^2\Psi}\right)$ is measured and substituted in equation 1

$$\sigma = \frac{-E\cos\theta}{1+\nu} \frac{\pi}{180} \frac{\Delta 2\theta}{\Delta sin^2\Psi} \quad (1)$$

Where,
σ = stress in MPa,
E = Young's modulus of the material under investigation,
ν = Poisson's ratio,
ɵ = pores angle.

Rubber Wheel Abrasion

A rubber wheel abrasion (RWA) testing machine in Compliance with ASTM-G65 Procedure was used to determine the three-body abrasive wear resistance. Here, the test samples are pressed against the circumferential portion of the rubber wheel, having a dimension of 228.0 mm diameter and a width of 12.7 mm. The silica sand (Figure 4) having AFS 60 (~ 210 μm) is fed from a nozzle at the interface of the sample, and the rubber where (Refer Figure 5), and the test is conducted for 6000 revolutions (200 rpm) at a load of 130 N. Before and after the tests, all the samples are cleaned in an ultrasonic bath and air dried. The weight of the sample before and after the test is noted, and the differences in the weight readings indicate abrasion loss. A minimum of three measurements are done, and the average value is reported.

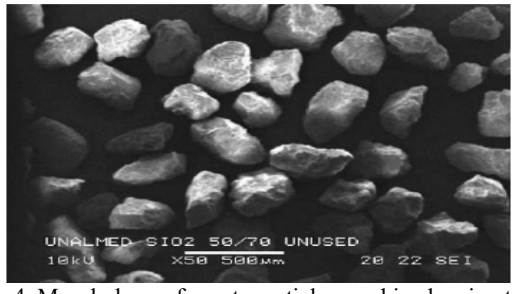

Fig. 4. Morphology of quartz particles used in abrasion tests

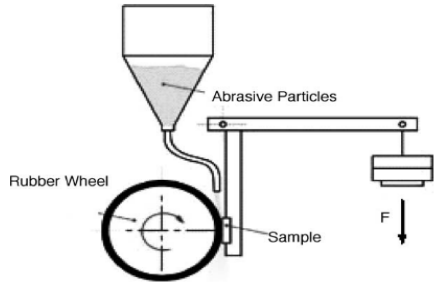

Fig. 5. Schematic of the dry Sand–rubber Wheel Testing machine, ASTM G65 standard

3. Results and Discussion

The test samples have been designated as shown in the Table 1 along with to the sample descriptions provided in the same table.

Table 1.
Sample description and designation [24]

Sl. No	Sample Description	Sample Identification
1	Mild steel cold rolled	MS
2	NiHard4	NH4
3	High Chromium Iron	HiCr
4	High Chromium Manganese Iron 5% Mn	HiCr5Mn
5	High Chromium Manganese Iron 10%Mn	HiCr10Mn
6	High Chromium Manganese Iron 15% Mn	HiCr15Mn

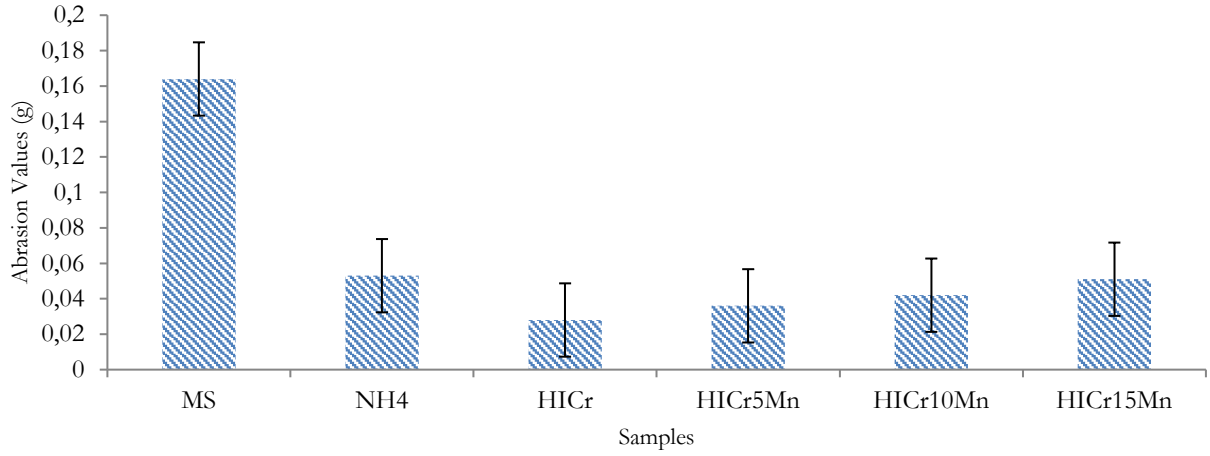

Fig. 6. Abrasion loss values of HiCr Iron Samples

Table 2.
Allocation of Hardness, RA content and CV% [27]

Sl. No	Sample Identification	Hardness				RA	CV
		Before Abrasion test		After Abrasion test			
		HRC	BHN	HRC	BHN		
1	MS		130		160		
2	NH4	49.5	468	51.0	486	68	14
3	HiCr	61.0	642	62.0	658	10	30
4	HiCr 5 Mn	59.0	613	60.0	627	52	26
5	HiCr 10 Mn	54.0	534	55.0	552	57	24.5
6	HiCr 15 Mn	50.0	469	51.0	486	62	23

Table 3.
Composition of the test samples analyzed Chemical Composition wt. % [27]

Sl. No	Material	C	Mn	Si	Cr	Ni	Mo
1	MS	0.16	0.58	0.22	-	-	-
2	NH4	3.10	0.56	1.58	9.20	5.20	0.20
3	HiCr	2.90	0.58	0.75	16.80	0.40	1.35
4	HiCr 5 Mn	2.22	5.53	1.68	17.16	1.08	1.23
5	HiCr 10 Mn	2.68	10.32	1.41	17.92	0.93	1.12
6	HiCr 15 Mn	2.78	15.42	1.27	18.17	0.80	1.33

Hardness Data

The hardness data before and after abrasion tests, Retained Austenite (RA) content, and Carbide Volume % (CV) are depicted in Table 2. As the test samples are subjected to surface grinding operation, high wear resistance and compressive stress are generated due to the plastic deformation and phase transformation involved [28, 29]. A heat treatment process follows this and ends up with higher hardness levels. During heat treatment, there will be changes in the microstructural features in the form of grain size reduction and phase transformation, such as lower Austenitic levels, etc.

From Table 2, it is observed that the hardness values obtained for MS are the lowest, and the highest value is obtained for the HiCr sample. The NH4 sample shows a hardness level of 49.5 HRC, which is much lower than that of HiCr (61 HRC). The hardness levels have gone up for the NH4 (51 HRC) and HiCr (62 HRC) samples after they undergo the abrasion process. The % increase in hardness of HiCr and NH4 after the abrasion test is 1.6 % and 3 %, respectively, over the corresponding un-abraded samples. These are on the expected lines in view of the fact that the samples are subjected to a work hardening process, resulting in an enhancement of the hardness level. This process can increase the hardness as the material undergoes plastic deformation due to the dislocations accumulating and interactions being enhanced. Also, the cohesive force between the particles/grains increases, which is controlled by the Vander wall forces, and the grain size morphological changes.

The % increase in hardness of (HiCr5Mn, HiCr10Mn, and HiCr15Mn) samples over un-abraded samples is 1.7 %, 1.85 % & 2 %, respectively. The increase in hardness may be due to the abrasion process taking place during three-body wear, which, on account of the deformation process, results in changes in the metallurgical phenomena.

Referring to Table 2, the RA content of HiCr is the lowest, and the highest RA is noted for NH4, followed by HiCr15Mn samples. The CV of NH4 shows the least and highest for HiCr. These data trends are getting very good support from the hardness data, where the higher the RA, the lower the hardness, and vice versa. Similarly, the analogy explained earlier for RA also holds good for CV %.Table 3 depicts the Chemical compositions of the test samples.

Abrasion Loss

The rubber wheel abrasion data with respect to different materials are shown in Figure 6. They represent abrasion volume loss data obtained during abrasion experiments. It is very well seen from Figure 6 that the abrasion loss of HiCr is the least, while MS shows the highest loss. The next highest is represented by NH4, followed by HiCr5Mn, HiCr10Mn, and HiCr15Mn, respectively. These abrasion loss values obtained match with the hardness values. The higher the abrasion loss, the lower the hardness and vis-à-vis. The HiCr shows the lowest value because of the presence of primary carbides in the hard matrix. However, MS, possessing a softer matrix (ferrite in pearlite), is contributing to higher abrasion loss.

The rest of the samples show abrasion losses, which are in between HiCr and MS. As observed from Figure 6, MS has the highest abrasion loss (~0.16). This behavior is attributed to its ferrite-pearlite microstructure, which lacks the hard carbides needed to resist abrasive wear effectively. The absence of reinforcing carbides causes MS to lose material quickly under abrasive conditions. HiCr, on the other hand, exhibits the lowest abrasion loss (~0.02). This excellent performance is due to its martensitic matrix reinforced with primary carbides (say, M7C3), which act as wear-resistant phases [30]. These carbides prevent material removal during abrasion, thereby improving the wear resistance. The presence of a strong matrix-carbide structure is a critical factor in its superior performance. In one of the investigations reported by Tabrett, [31] on the abrasion wear resistance of Ni-Mo alloyed high chromium irons subjected to destabilization heat treatment at 900°C for one hour and cooled to room temperature followed by tempering at 450°C/600°C for 6 hours, and compared the abrasion data with as-cast which is predominantly austenitic structure. The latter exhibited better abrasion resistance over destabilized samples with a carbon content of 3.95% owing to the high hardness obtained for the other alloy containing 2.94% C. The heat treatment has a better effect in improving the hardness & abrasion wear resistance due to the occurrence of phase transformation and variations observed in the carbide morphological features. The Figure 6 also highlights the intermediate performance of NH4 and HiCrMn alloys (HiCr5Mn, HiCr10Mn, and HiCr15Mn). As manganese content increases, the amount of retained austenite in the matrix rises, reducing hardness and increasing abrasion loss. For example, HiCr15Mn shows a higher abrasion loss (~0.05) compared to HiCr5Mn (~0.03) due to the increased proportion of softer retained austenite, which compromises wear resistance. From this study, it is inferred that the composition and type of heat treatment have a bearing on the final properties. In the present case, HiCr in the heat-treated condition has also revealed the best abrasion resistance properties compared to other samples studied, i.e., HiCr5Mn, HiCr10Mn, HiCr15Mn, and NH4.

The data from Figure 6 strongly supports this observation, as the heat-treated HiCr achieves the lowest abrasion loss due to its optimized carbide structure and hard martensitic matrix. This demonstrates that both alloy composition and controlled heat treatment are critical for enhancing wear resistance. Hence, the abrasion data obtained is getting very good backing from the hardness levels. This type of work has hardly been reported in the literature, considering all these parameters, and hence, it has been attempted for the first time in this sphere of work. In the earlier work reported [27], it is seen that HiCr15Mn possesses better impact resistance and lower hardness compared to HiCr5Mn sample. This trend is on the expected lines because of higher austenite retention and lower carbide volume and gives very good support to the literature aspects. This trend is also evident in the graph, where HiCr15Mn shows higher abrasion loss due to the trade-off between impact resistance and wear resistance. This trade-off highlights the importance of optimizing the balance between hardness and toughness in these alloys for different applications.

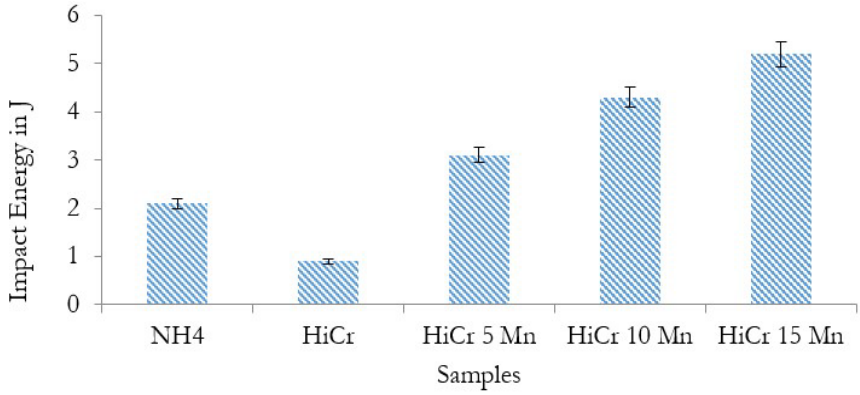

Fig. 7. Impact Energy values of HiCr Iron Samples

Impact Energy

The impact energy data collected for the tested samples, are presented in the bar diagram in Figure 7, provide valuable insights into the mechanical properties of different alloy compositions. Impact energy is a critical measure of a material's ability to absorb energy during deformation or fracture, which directly relates to its toughness and resilience. Higher impact energy indicates that a material can withstand more shock or sudden forces without breaking. This property is especially important for materials used in impact-prone environments, such as machinery components and construction equipment. In this study, the HiCr15Mn sample demonstrated the highest impact energy among all tested samples, recording a value of 5.2 Joules. This indicates that the HiCr15Mn alloy possesses superior toughness and is more resilient under impact loading compared to the other materials tested. The addition of 15% manganese (Mn) significantly improves toughness by stabilizing retained austenite in the microstructure. Retained austenite can absorb energy during impact by transforming into martensite, a harder phase, which helps dissipate impact forces effectively.

In contrast, the HiCr sample, which lacks manganese, exhibited the lowest impact energy among the tested samples. This lower impact energy indicates that the HiCr alloy is more brittle and less capable of absorbing energy during impact, making it less suitable for applications where high toughness is required. The absence of manganese limits the formation of retained austenite, resulting in a predominantly martensitic structure that is hard but brittle. This makes HiCr prone to fracturing under sudden impact forces. The HiCr5Mn sample, with a recorded impact energy of 3.1 Joules, shows an intermediate level of toughness. While the addition of 5% manganese has improved its impact energy compared to the HiCr sample, it still falls short of the toughness demonstrated by the HiCr15Mn sample.

Similarly, the Ni-hard 4 (NH4) sample displayed a relatively low impact energy of 2.1 Joules. Ni-hard alloys are typically known for their hardness and wear resistance rather than their toughness. The low impact energy of the NH4 sample aligns with this characteristic, indicating that while the material may perform well in applications requiring high hardness and wear resistance, it may not be the best choice for scenarios where impact resistance is critical. As observed in Figure 7, the steady increase in manganese content from HiCr5Mn to HiCr15Mn shows a direct improvement in impact energy. This trend highlights the role of manganese in altering the microstructure, specifically by increasing the retained austenite volume, which enhances the ability of the material to absorb shock loads effectively. These variations in impact energy among the tested alloys highlight the influence of compositional changes, particularly the addition of manganese, on the mechanical properties of the materials. The HiCr15Mn sample's superior performance underscores the significant role of manganese in improving impact resistance, making it a more resilient option for applications where materials are subjected to sudden or repeated impact forces. The results also emphasize the importance of balancing toughness and hardness, as materials with higher manganese content may exhibit slightly lower hardness due to the increased proportion of softer austenitic phases. This trade-off must be optimized for specific engineering applications. Overall, the findings suggest that the addition of manganese can lead to a marked improvement in the toughness of materials, potentially expanding their usability in demanding engineering applications. This also indicates that controlled manganese addition can help tailor the properties of high-chromium iron alloys to meet diverse application needs, ranging from high-impact resistance to superior wear performance.

Residual Stress

The results pertaining to RS before and after the abrasion test for the samples are given in Figure 8. It is observed from Figure 8 that HiCr samples exhibit the highest level of compressive stress (CS), whereas MS exhibits the least. The stress pattern remains the same for all samples before and after they are subjected to an abrasion test. These trends obtained are attributed to the carbide morphological features as well as matrix structure that prevailed in the samples, which are discussed under the section "light microscopic features. The HiCr shows a predominantly martensitic structure compared to NH 4, which shows the presence of austenitic and martensitic. Thus, the RS value measured is of compressive type (355 MPa) with a higher magnitude compared to NH4, which shows RS values of 38.79 MPa. This significant difference is attributed to the finer grain structure in HiCr, which strengthens the material and allows for higher compressive stress levels. Martensitic transformations during heat treatment further contribute to compressive stress by increasing the material's density and creating internal resistance to deformation. In all these cases, the reliability factor is ±20 MPa.

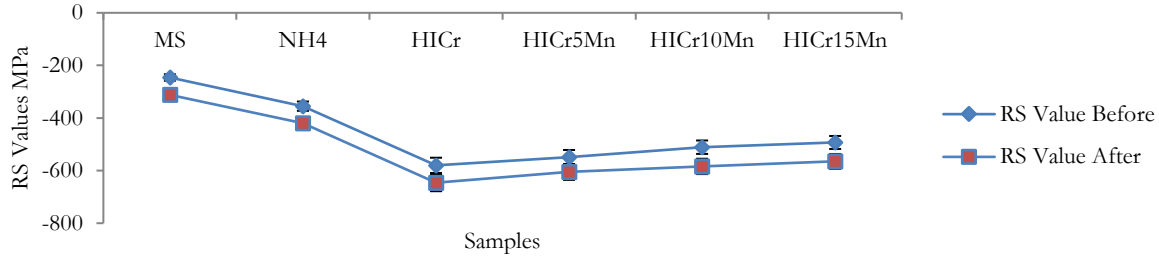

Fig. 8. Residual stress data before and after abrasion of Ni-Cr Iron Samples

The MS shows ferrite in perlite, which is much coarser than HiCr and NH4; it is known that the finer the grain size, the better the properties. Finer grain structures in HiCr and NH4 provide higher grain boundary density, which acts as barriers to dislocation motion

during stress application. This results in higher compressive stress values. In contrast, MS has a coarser grain structure, leading to lower RS values. As HiCr exhibits a fine-tempered martensitic structure and finer carbide precipitation, it achieves higher hardness and lower retained austenite, resulting in higher compressive stress. The other samples, HiCr5Mn, HiCr10Mn, and HiCr15Mn, are showing RS in the range of 93 to 91 MPa with a reliability factor of ±20 MPa. The gradual reduction in retained austenite content as manganese content decreases in HiCrMn alloys plays a crucial role in increasing RS values. Lower austenite levels enhance the martensitic matrix, which increases the resistance to deformation under compressive forces.

It is known that higher compressive stress is induced in metal parts following heat treatment due to phase transformation and finer grain formation. In the present case, higher CS is noticed in HiCr samples compared to NH4 samples, as well as in HiCr5Mn over HiCr15Mn samples, and the reason may be attributed to the reduction in austenite content. This phenomenon aligns with the Hall-Petch relationship, where smaller grain sizes result in increased yield strength and compressive stress due to reduced grain boundary spacing.

As reported in the published work carried out by Pramod [32], in HiCrMn samples with a section size of 12 mm, the sample with 5% Mn showed higher CS compared to samples with 10% Mn. This was attributed to a finer carbide network, lower carbide volume, and reduced retained austenite content. In the current study, similar behavior is observed, as HiCr5Mn displays higher CS than HiCr15Mn. The reduced carbide size and optimized distribution of carbides in HiCr5Mn improve its load-bearing capacity, resulting in higher compressive stress. Albertion and Sintora [12], in their investigation done on abrasion resistance on steels and chromium irons used in mining applications, have reported the addition of niobium alloy yielded the best result, and the reasons have been attributed to shape, size, and distribution of niobium carbides in the matrix and finally engineered the alloy configuration. In this work also, the adoption of chromium carbides in Nihard, HiCr, and HiCrMn samples is mainly responsible for the enhancement in wear resistance; this is in agreement with the literature report [32]. The high-stress abrasion studies were carried out by Lindroos [33] on high-strength steels using scratch test devices. The result has revealed the fact that the surface hardness saturates to a certain applied load, which is high enough to influence wear behavior due to the work hardening process and microstructural aspects such as the formation of phases, etc., This saturation in hardness occurs because, under high applied loads, the material undergoes plastic deformation that induces dislocation multiplication and creates a denser dislocation network, which strengthens the surface. In this investigation, it is also seen that the work-hardening effects have been observed in Ni-Cr irons, as evidenced by the hardness values. The abrasive action during testing enhances surface hardness by introducing dislocations and refining the microstructure. This contributes to improved wear resistance by making the material more capable of withstanding further abrasive forces. Thus, the work done and the literature reports [27, 31, 32] agree with each other. The work hardening ability of high manganese steel during compression has been investigated by Pei [34], where it is reported that microstructurally, the steel produced twins and slip during compression has increased hardness and a decrease in dislocation density. The formation of twins enhances the material's capacity for plastic deformation, while slip bands increase the localized strength of the material. It has produced a work-hardening effect on steel, thereby increasing the hardness and increasing plastic deformation with an increase in dislocation density. In the current study, a similar mechanism of twinning and slip may contribute to the increased hardness observed in HiCrMn samples. These microstructural features not only improve hardness but also enhance the overall wear resistance. In the present case also, the work hardening effect due to abrasive action has increased the hardness, like the work reported [35], emphasizing the fact that the work hardening process has a positive effect on the hardness in wear-resistant irons. This increase in hardness due to work hardening is particularly effective in Ni-Cr irons, where the martensitic matrix is further strengthened through dislocation interactions, improving their performance under abrasive conditions. The effect of laser surface hardening on RS has been studied [36], wherein structure-property correlations have been established.

Further, higher compressive stress has been found in the hardened area where the martensitic structure is observed as a consequence of volume changes occurring during the transformation. This phenomenon occurs because the martensitic transformation involves an increase in volume, which generates internal stresses that resist deformation and increase the material's compressive stress levels. In the present work, compressive stress has also been developed for the predominant martensitic structure obtained in HiCr samples, followed by HiCr5Mn, HiCr10Mn, HiCr15Mn, and NH4. The presence of martensite provides high compressive stress, as it is a hard phase capable of withstanding high loads and resisting crack propagation. This trend further confirms the correlation between microstructural features, like martensite and carbides, and residual stress behavior. Based on this exercise, it is inferred that the martensitic transformation results in generating compressive stress. This compressive stress not only improves the material's ability to resist wear but also increases its fatigue resistance, making it highly suitable for applications involving repeated loading or high-abrasion conditions.

Optical Microscopic Feature

Figure 9a-f, respectively, show light micrographs of samples as listed in Table 1. Figure 9a shows the microstructure of the MS sample, which reveals ferrite grains in the perlite matrix. The grains are very well distributed in the perlite matrix with equal axial grains. By looking at the micrograph, it could be easily observed that the ferrite phase (light-colored regions) is soft and ductile. In contrast, the pearlite phase consists of alternating layers of ferrite and cementite, which make it harder and stiffer. This dual-phase microstructure offers toughness as well as strength. The grains having equal axial distribution indicate isotropic mechanical properties in any direction that is needed to achieve by applications. The observed ferrite grains, with smooth boundaries, suggest that the MS sample has good plasticity and moderate toughness, making it suitable for structural applications. However, due to the absence of carbides or a martensitic matrix, the wear resistance is expected to be lower compared to alloys like HiCr, which exhibit more complex and harder microstructures.

Now, coming to NH4 in the heat-treated condition, the microstructure in Figure 9b reveals the presence of discontinuous carbides in a martensitic matrix. The RA (retained austenite) and

CV (carbide volume) values obtained are 65% and 14%, respectively. As the RA value is much higher, the hardness value has come down to 49 HRC. The discontinuous carbides do impart some hardness but are insufficient to fully compensate for the softening effect caused by the high retained austenite content. Retained austenite is a softer phase that lowers the overall hardness of the matrix, which explains why the hardness value obtained is lower. The martensitic matrix is there but is less effective because the high RA content dilutes its strengthening effects.

Figure 9c shows the microstructure of heat-treated HiCr samples, which comprises a fine-tempered martensitic structure along with the presence of eutectic carbides. The RA and CV obtained for the sample are 10% and 30%, respectively. As the RA value is much lower and depicts a predominant martensitic structure, the hardness value has gone up, which is on the expected lines [37]. The eutectic carbides form strong reinforcing phases within the matrix, opposing deformation and adding considerably to the hardness and wear resistance of the material. The tempered martensitic structure also helps in toughness so that it is balanced by hardness as well as impact resistance. The uniform dispersion of carbides within the matrix further enhances the mechanical properties, especially under abrasive conditions.

In the microstructure of HiCr iron, the main carbides present are of primary type and varied sizes, with some hexagonal shapes in an austenite matrix. These carbides are dispersed randomly within the matrix, and the value obtained is in agreement with the hardness value reported in Table 4. The random dispersion of carbides ensures that during loading, the stress is dispersed throughout the matrix and, thus, less likely to cause localized deformation or cracking. The hexagonal carbides are particularly effective in resisting wear due to their high hardness and stability under stress, though their geometry is unique. The austenite matrix is softer than martensite, but it provides the necessary ductility to absorb impact energy, so the material does not become overly brittle.

The HiCr5Mn, HiCr10Mn, and HiCr15Mn microstructures exhibited in Figures 9d-f, respectively, are considered for discussion. The HiCr5Mn sample features an austenitic phase with a hardness of 59 HRC. The micrograph reveals the presence of a finer carbide distribution within the austenitic matrix, which enhances hardness and wear resistance. The relatively lower RA content of HiCr5Mn lets the martensitic transformation take place more effectively under deformation, and this translates into better mechanical performance during abrasion. A hardness value of 54 HRC characterizes the austenitic matrix in the sample HiCr10Mn. This sample contains longer carbides, including hyper-eutectic hexagonal carbides, distributed within the matrix. These carbides constitute reinforcing phases and consequently improve wear resistance, yet they do not lose their hardness after abrasion testing. The higher RA content in HiCr10Mn than in HiCr5Mn reduces the hardness of the former a little but gives a good balance between toughness and abrasion resistance. The geometry of hexagonal carbides is particularly efficient in resisting wear due to the distribution of stress at the loading point. The sample HiCr15Mn has higher austenitic content with a hardness level of 50 HRC. The micrograph reveals the presence of larger and longer carbides, including hyper-eutectic carbides, in an austenitic matrix. The higher RA content of 62% results in a softer matrix, which lowers hardness but increases impact resistance. Although the CV of 23% offers some degree of reinforcement, the dominance of austenite limits the material's hardness compared to HiCr5Mn and HiCr10Mn. However, this composition makes HiCr15Mn better suited for applications requiring toughness over extreme hardness. Thus, there is a very good relationship existing between RA and CV, as well as the microstructure. For HiCr15Mn samples, 62% RA and 23% CV correlate well with the observed hardness and wear resistance. The retained austenite is a source of a stress-induced transformation, which raises toughness but reduces hardness.

The tradeoff is self-evident with the HiCrMn samples in that an increased manganese content reduced hardness but improved RA, creating differences in the wear resistance and performance. HiCr10Mn with 10% Mn presents long carbides with hyper-eutectic hexagonal carbides within the austenitic matrix of 55% RS with abrasion values of 0.042 before tests and 0.033 after. The measured hardness is recorded as 54.0 and 55.0 HRC before and after the abrasion test, respectively. The slight increase in hardness post-abrasion indicates a work-hardening effect, where dislocation movement and carbide reinforcement improve the matrix's resistance to wear. HiCr15Mn, with 15% manganese content, shows larger, longer carbides with hyper-eutectic carbides of bigger size in the austenitic matrix with 62% RA. Hardness measured is 50.0 and 51.0 HRC before and after abrasion tests. The bigger size of the carbide contributes to toughness while reducing the hardness in total comparison to the finer carbide distribution found in HiCr5Mn. Once more, this indicates that a small hardness gain post-abrasion evidence of work-hardening properties of the material under stress.

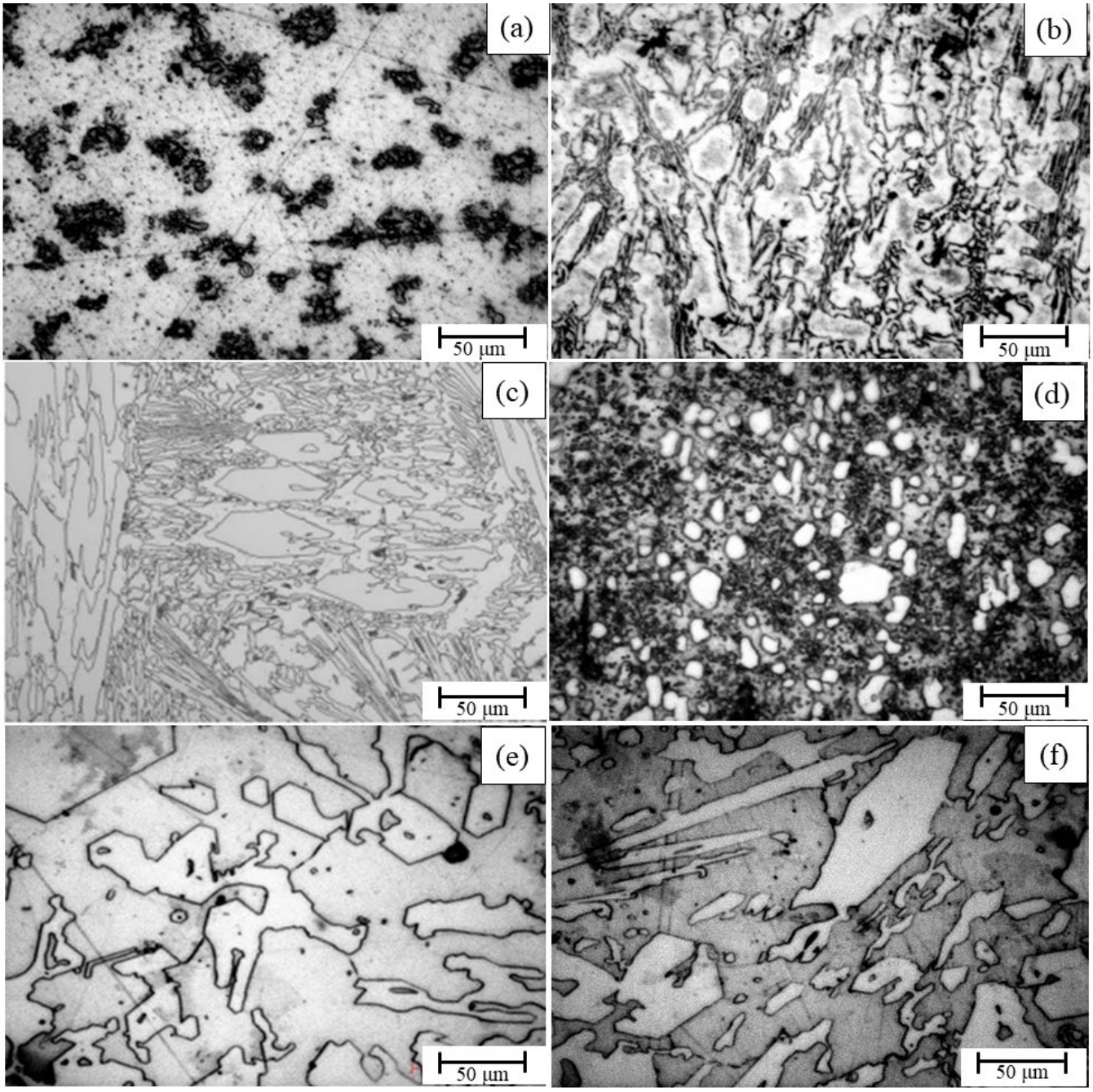

Fig. 9. Optical microscopic of different materials (500 x): a) MS sample, b) NH4 sample, c) HiCr sample, d) HiCr5Mn sample, e) HiCr10Mn sample, and f) HiCr15Mn sample

These micrographs elucidate the structure of the matrix. Size, distribution, and matrices with morphology are of significance regarding properties of HiCr5Mn, HiCr10Mn, and HiCr15Mn. The material performance can be directly associated with size-carbides—harder and better resistance toward wear is presented when the size is smaller. Larger sizes, such as HiCr15Mn, reduce hardness while raising toughness. The microstructural features are reported to play a crucial role in determining the characteristics of the HiCr family, as supported by literature reports [38, 39, 40]. Uniform carbide distribution observed in HiCr5Mn and HiCr10Mn minimizes localized stress concentrations, thus ensuring better wear resistance and uniform mechanical behavior. The type of matrix (martensitic or austenitic) also governs the material's hardness and toughness. For example, HiCr5Mn, with its tempered martensitic matrix, achieves higher hardness, whereas the higher austenite content in HiCr15Mn provides better impact resistance.

In summary, it is summed that the abrasion loss data correlates with residual stress and hardness data before and after the abrasion tests. They are further dependent on the microstructural features, especially martensitic matrix, carbide features such as size, and their distribution in the matrix.

Fractography of Impact Tested samples

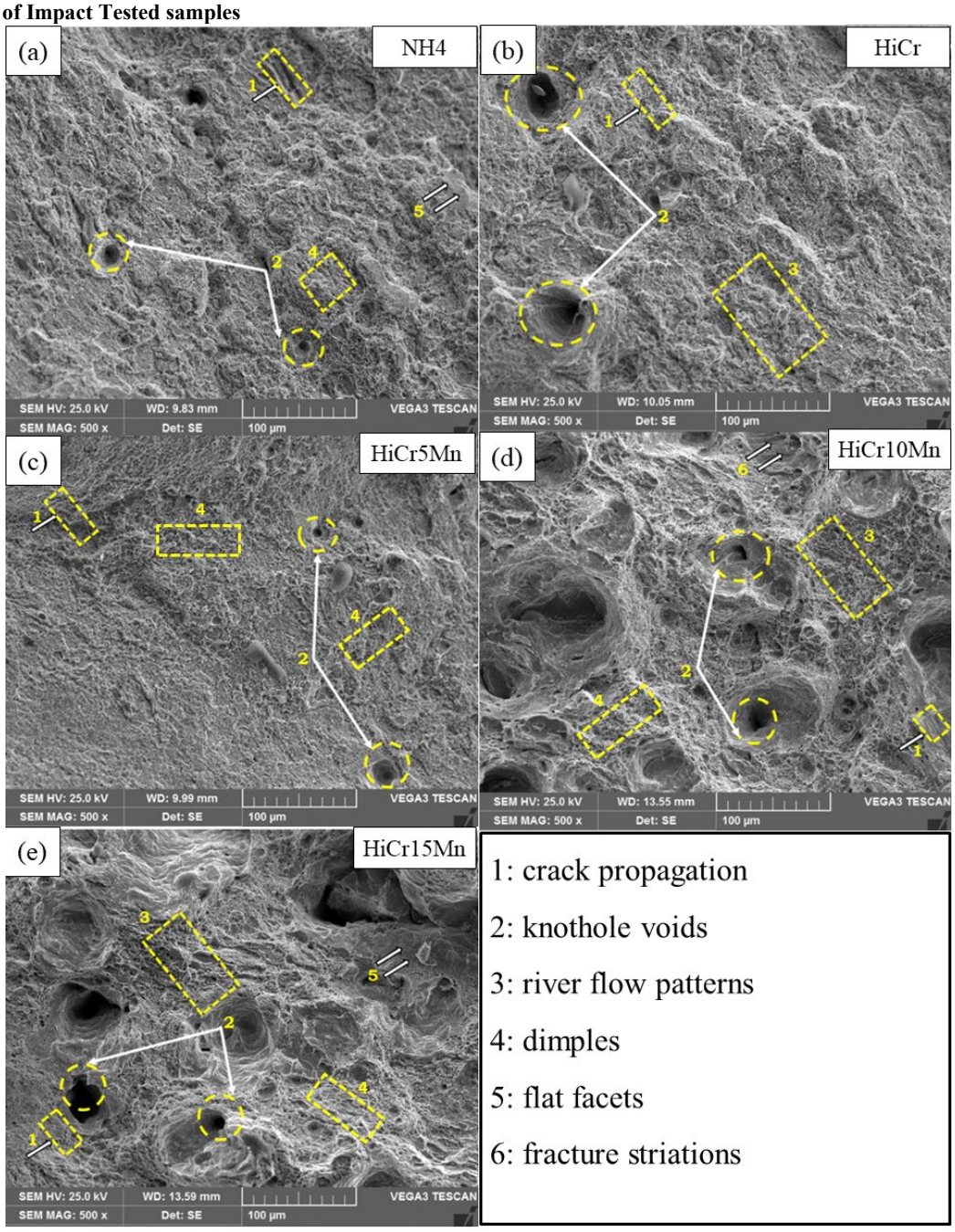

Fig. 10. Fractography analysis of different materials (500 x): a) NH4 sample, b) HiCr sample, c) HiCr5Mn sample, d) HiCr10Mn sample, and e) HiCr15Mn sample

The fractography images of impact-tested samples, as detailed in Table 1, are presented in Figures 10 a-e. These figures represent different fracture characteristics, such as crack propagation, knothole voids, river flow patterns, dimples, flat facets, and fracture striations, all of which represent different fracture mechanisms.

Figure 10 showcases the impact fractographs of Ni-hard 4 (NH4) samples. The rupture surface is largely depicted by dimples, revealing a ductile breakage mode. These dimples indicate that the material endured considerable distortion prior to fracture. They are caused by the nucleation, advancement, and amalgamation of microvoids during plastic distortion [41, 42, 43]. Dimples are evident in this fractograph as the characteristic of ductile fracture. The size and uniformity suggest a material with medium toughness, which can absorb high energy before failure. It is characteristic of materials having a softer matrix, such as NH4, where ferrite or pearlite may permit localized plastic deformation.

Additionally, knothole voids are present in certain regions, indicating localized areas of material separation. These pores often occur due to inclusions, carbide pullouts, or local stress concentrations in the impact process. The existence of such pores indicates that some regions of the material could be weaker or contain structural heterogeneities, acting as sites for crack initiation. The presence of flat facets in certain zones prompts the onset of localized brittle fracture zones within the otherwise ductile matrix. These facets are probably due to areas with more carbide concentration or regions of microstructural inhomogeneity. While the overall matrix would be ductile, these localized brittle regions could compromise the material's overall toughness under high-stress conditions.

Figures 10b and c show the effect fractographs of High Chromium (HiCr) and High Chromium with 5% Manganese (HiCr5Mn) samples, respectively. The fracture surfaces in these images are similar to those observed in Figure 10. Dimples are again dominant, indicating a ductile fracture mode, with knothole voids spread over the fracture surface.

In Figure 10 (HiCr sample), dimples are sharper and better distributed than those in NH4, thus indicating that the fracture mechanism is better controlled. In HiCr, the dimple refinement is attributed to the combination of the martensitic matrix and the reinforcement effect of carbides. Nevertheless, the size of knothole voids is larger in HiCr than in NH4, meaning that before the final fracture, plastic deformation occurred at higher levels of stress concentrations during the impact event. This behavior agrees well with the increased hardness of HiCr and its stress at failure.

In Figure 10, the HiCr5Mn sample appears to be a mixture of dimples and knothole voids, but as can be seen, it is larger compared to HiCr. Manganese in the fracture surface may support the enhancement of plastic deformation due to the higher-sized void. Manganese enables twinning and slip phenomena that take place when such a material is undergoing deformation; hence, more energies can be absorbed prior to fracturing. This is because of the balance of hardness and toughness coupled with the malleable features that appear more on the fracture surface. Significantly, the size of voids in the samples is larger compared to that of the NH4 sample. This suggests greater plastic deformation or perhaps a different microstructural response under impact loading. The large sizes of the voids in both HiCr and HiCr5Mn samples serve as points of concentration of stress. Therefore, the tendency for fracture under continued loading is increased. However, the refined dimple morphology in both samples ensures delayed crack propagation, contributing to their enhanced mechanical performance.

Figures 10d and e, provide the impact fractographs of High Chromium with 10% Manganese (HiCr10Mn) and High Chromium with 15% Manganese (HiCr15Mn) samples, respectively. The fracture surfaces in these images show the presence of river flow patterns, voids, flat facets, and fracture striations. The river flow patterns characterized by wavy, parallel lines are indicative of brittle fracture propagation along specific crystallographic planes. These are indicative of fracture in the regions dominated by cleavage, where material fails along preferred atomic planes under stress. The sharper and more pronounced these patterns are, the larger the brittleness in localized zones. The presence of voids indicates limited ductile failure. The void sizes are larger in HiCr15Mn than in HiCr10Mn, indicating higher levels of plastic deformation in this material. The greater amounts of retained austenite, likely in HiCr15Mn, promote plastic deformation, so more energy is absorbed before fracture. The flat facets suggest brittle cleavage regions. These facets correspond to areas of sudden failure because of stress concentrations, probably at carbide clusters or grain boundaries. The bigger and more developed facets in HiCr10Mn suggest a higher volume fraction of carbide, which increases the strength of the matrix but creates localized brittleness. Fracture striations are typical of impact damage -like features where crack propagation was stepwise. The presence of striations in these samples suggests repeated stress application or impact-induced defects. This behavior highlights the mixed response of the material, where there are ductile regions accommodative of plastic deformation and brittle regions failing along preferred paths. The coexistence of the features suggests a mixed-mode fracture mechanism, where both the ductile and brittle behavior contribute to the overall fracture process. With somewhat lower retained austenite and higher carbide volume, HiCr10Mn tends toward brittle fracture more, as suggested by a deep river flow pattern and faceted morphology.

On the contrary, the more balanced manifestation of ductile and brittle behavior is expected in the case of HiCr15Mn due to larger voids, higher retained austenite, and subsequent higher energy dissipation associated with fracture. In summary, Figures 10a–c are found to be mostly characteristic of ductile fracture, with primary features being dimples and knothole voids. In contrast, Figures 10d and e indicate a more complex mode of fracture involving ductile and brittle failure processes. The transition from the ductile to the mixed-mode fracture process with the increase in manganese content shows how alloy composition plays a strong role in determining the modes of fracture in these materials in impact loading conditions.

Wear track of impact tested samples

Figure 11a shows that the Mild Steel (MS) sample has a wear track with broad grooves accompanied by pronounced material deformation. The wear track is dominated by an abrasive wear mechanism, as evidenced by clear plowing marks along the wear track that result from hard asperities from the counter surface interacting with the MS sample to displace material through abrasive action. This behavior is typical of soft materials with limited hard phases, where surface damage primarily results from material removal rather than resistance to cutting forces. These

findings indicate the MS sample's susceptibility to considerable surface strain and deformation under abrasive wear condition, emphasizing its limited resistance to abrasive forces.

On the other hand, the wear track of the NH4 sample (Figure 11b) is relatively smoother with parallel, finely etched grooves in which the sliding direction is parallel as well. This pattern hints at mild abrasive wear supported by sliding and no occurrence of severe deformation that seems to indicate improved surface durability in impact conditions than that offered by the MS sample. The reduced deformation implies that the NH4 sample possesses improved resistance to surface strain induced by repeated impacts, highlighting a favorable balance between hardness and ductility. The presence of a martensitic matrix and finely dispersed carbides significantly contributes to NH4's superior wear resistance compared to MS, allowing it to resist surface damage more effectively. The High Chromium (HiCr) sample's wear track is illustrated in Figure 11c. It contains sharp, narrow grooves, which are all very closely aligned to the sliding direction and are a typical feature of abrasion with limited material movement. Such wear patterns that contain clear groove features with limited plastic deformation correspond well with the surface hardness imposed by chromium. The presence of hard, uniformly distributed carbides within a martensitic matrix significantly enhances the surface's ability to resist cutting and plowing actions. Chromium's hardening effect appears to enhance the sample's resistance to plastic flow and abrasive forces, demonstrating that the HiCr sample is better equipped to withstand abrasive wear with minimal surface degradation under impact testing conditions.

Figure 11d. SEM micrograph of the HiCr5Mn sample showing long, continuous grooves parallel to the sliding direction, indicating primarily abrasive wear. Grooves are more pronounced than in the HiCr sample, suggesting a slight compromise in hardness by the addition of 5% manganese, with possibly an increase in toughness. Manganese promotes localized plasticity and surface work-hardening, which helps the material absorb energy during deformation, though at the cost of slightly reduced wear resistance compared to HiCr. Evidence of slight material displacement implies that wear resistance is moderately reduced compared to the HiCr sample. The HiCr10Mn sample's wear track is seen in Figure 9e and exhibits wider and less uniform grooves with visible plastic deformation along the track. The increased manganese content enhanced toughness but slightly reduced hardness, thus resulting in noticeable displacement and plastic flow under impact forces. This wear track shows signs of both abrasion and adhesion mechanism, suggesting the possibility of material transfer from the HiCr10Mn sample to the counter surface. This dual mode of wear indicates an increase in manganese levels, resulting in a more ductile alloy that, though able to absorb energy more efficiently, can withstand much less localized damage to the surface under intense impact.

Figure 11f The HiCr15Mn sample shows the most complicated wear track. There are deep grooves and pits with evident signs of sharp damage on the surface. Its morphology represents a combination of three types of wear mechanisms, namely abrasion, adhesion, and impact. The high Mn concentration confers high toughness on this material but excessive ductility, which appears to make its surface more susceptible to impact deformation. The pits and micro-cracks observed along the wear track suggest that the high ductility allows crack initiation and propagation, further compromising the surface's resistance to repeated impacts. The presence of micro-cracks and surface fractures suggests that the HiCr15Mn sample's wear resistance is compromised due to its pronounced ductility, leading to substantial surface degradation and making it the most vulnerable sample among those tested.

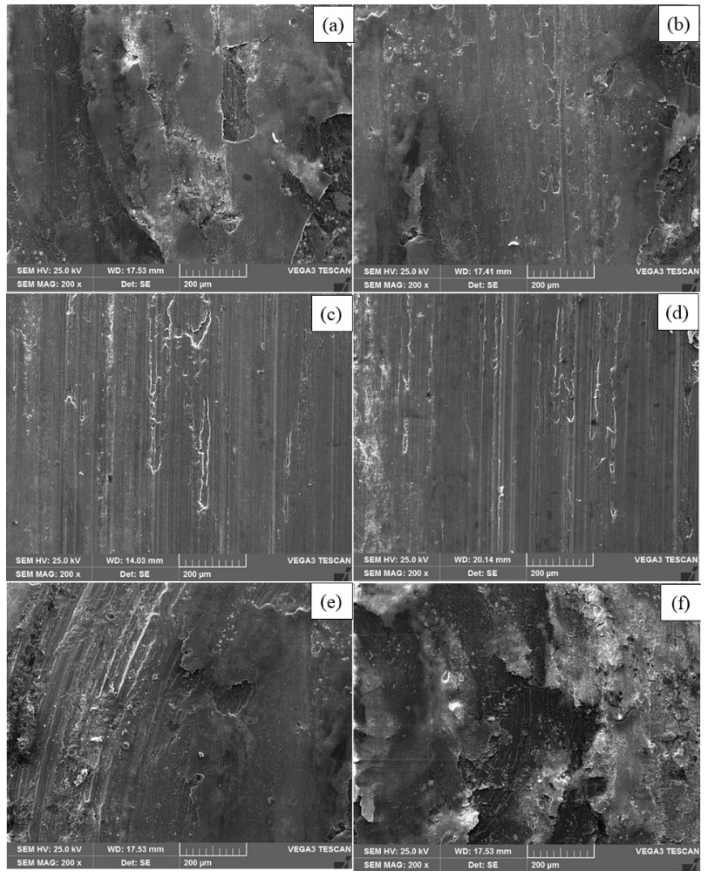

Fig. 11. Wear Track of different material (200 x): a) MS sample, b) NH4 sample, c) HiCr sample, d) HiCr5Mn sample, e) HiCr10Mn sample, and f) HiCr15Mn sample

Conclusion

Based on the investigation done for NH4, HiCr, and HiCrMn samples on abrasion loss and RS, the following important points emerge: the samples considered for this work are in the heat-treated condition.

- The HiCr sample displays the highest hardness, followed by NH4, HiCr5Mn, HiCr10Mn, and HiCr15Mn samples.
- The abrasion loss of HiCr is shown to be the lowest; on the other hand, HiCr5Mn is exhibiting the highest of the others in between them.
- HiCr samples feature the highest CS, followed by NH4, HiCr5Mn, HiCr10Mn, and HiCr15Mn samples.
- The microstructure features give very good support in terms of phase formation (RA), carbide volume fraction (CV), and their characteristics.
- The impact fractographs reveal a transition from predominantly ductile fracture in NH4, HiCr, and HiCr5Mn samples, characterized by dimples and voids, to a mixed-mode fracture in HiCr10Mn and HiCr15Mn samples, featuring river flow patterns, flat facets, and striations. This shift highlights the influence of increased manganese content on fracture behavior. Overall, higher Mn content introduces more brittle characteristics into the fracture process.

It may be deduced that the microstructural features are giving very good credence to the hardness, abrasion, and RS data in terms of the formation of phases and carbide morphologies and revealing the fact that HiCr is the best abrasion-resistant material possessing higher CS, lesser RA%, and Higher CV %. Among the HiCr Mn samples studied, HiCr5Mn reveals the best abrasion resistance with lower RA and higher CV as well as higher Hardness, compared to the other two samples. For the application involving superior abrasion resistance property, The RS, having the highest compressive stress, is the preferred choice to obtain a higher wear life expectancy of a part. Among HiCrMn samples, HiCr5Mn is preferred for abrasion resistance application; on the other hand, HiCr15Mn may be suitable in the field, possessing better resistance to impact.

References

[1] Lakkannavar, V., Yogesha, K.B., Prasad, C.D. & Prasad, C. (2024). Investigation of cyclic oxidation and hot corrosion behaviour of plasma-sprayed NiCrAlY/Cr3C2/h-BN/Mo coatings on T22 boiler steel alloy. *Journal of Bio-and Tribo-Corrosion*. 10(4), 85, 1-18. https://doi.org/10.1007/s40735-024-00890-w.

[2] Purushotham, N., Parthasarathi, N.L., Babu, P.S., Sivakumar, G. & Rajasekaran, B. (2023). Effect of thermal expansion on the high temperature wear resistance of Ni-20% Cr detonation spray coating on IN718 substrate. *Surface and Coatings Technology*. 462, 129490, 1-13. https://doi.org/10.1016/j.surfcoat.2023.129490.
[3] Shafranov, A.V., Morozov, E.A., Muratov, K.R., Ablyaz, T. R., Drozdov, A.A., Kornilov, A.A. & Lukin, E.V. (2021). Production of nickel–chromium coatings from powder by laser cladding. *Russian Engineering Research*. 41(5), 457-459. https://doi.org/10.3103/S1068798X21050208.
[4] Chen, W.C., Teng, F.Y. & Hung, C.C. (2014). Characterization of Ni–Cr alloys using different casting techniques and molds. *Materials Science and Engineering*. C, 35, 231-238. https://doi.org/10.1016/j.msec.2013.11.014.
[5] Yun, C.S., Hanawa, T., Hong, M.H., Min, B.K. & Kwon, T.Y. (2021). Biocompatibility of Ni–Cr alloys, with the same composition, prepared by two new digital manufacturing techniques. *Materials Letters*. 305, 130761, 1-4. https://doi.org/10.1016/j.matlet.2021.130761.
[6] Karimihaghighi, R. & Naghizadeh, M. (2023). Effect of alloying elements on aqueous corrosion of nickel-based alloys at high temperatures: A review. *Materials and Corrosion*. 74(8), 1246-1255. https://doi.org/10.1002/maco.202213705.
[7] Zhang, X. (2024). Modification and characterisation of nickel-based alloy materials for ultra-supercritical power generation. *Journal of Physics: Conference Series*. 2808(1), 012005. DOI: 10.1088/1742-6596/2808/1/012005.
[8] Tan, C., Krishnan, K. & Elumalai, N.K. (2024). Corrosion behaviour of heat-treated cold spray nickel chromium/chromium carbides. *Metals*. 14(10), 1153, 1-28. https://doi.org/10.3390/met14101153.
[9] Umanskyi, O.P., Storozhenko, M.S., Baglyuk, G.A., Melnyk, O.V., Brazhevsky, V.P., Chernyshov, O.O., Terentiv, O.E., Gubin, Yu.V., Kostenko, O.D. & Martsenyuk, I. S. (2020). Structure and wear resistance of plasma-sprayed NiCrBSiC–TiCrC composite powder coatings. *Powder Metallurgy and Metal Ceramics*. 59, 434-444. https://doi.org/10.1007/s11106-020-00177-y.
[10] Amanov, A. & Berkebile, S.P. (2023). Enhancement of sliding wear and scratch resistance of two thermally sprayed Cr-based coatings by ultrasonic nanocrystal surface modification. *Wear*. 512-513, 204555, 1-19. https://doi.org/10.1016/j.wear.2022.204555.
[11] Tabatabaeian, A., Ghasemi, A.R., Shokrieh, M.M., Marzbanrad, B., Baraheni, M. & Fotouhi, M. (2022). Residual stress in engineering materials: a review. *Advanced Engineering Materials.* 24(3), 2100786, 1-28. https://doi.org/10.1002/adem.202100786.
[12] Toboła, D. (2022). Influence of sequential surface treatment processes on tribological performance of vanadis 6 cold work tool steel. *Wear*. 488-489, 204106, 1-12. https://doi.org/10.1016/j.wear.2021.204106.
[13] Kaimkuriya, A., Sethuraman, B. & Gupta, M. (2024). Effect of physical parameters on fatigue life of materials and alloys: A critical review. *Technologies.* 12(7), 100. https://doi.org/10.3390/technologies12070100.
[14] Zhai, W., Bai, L., Zhou, R., Fan, X., Kang, G., Liu, Y. & Zhou, K. (2021). Recent progress on wear-resistant materials: designs, properties, and applications. *Advanced Science.* 8(11), 2003739. DOI: 10.1002/advs.202003739.
[15] Han, X., Zhang, Z., Wang, B., Thrush, S. J., Barber, G. C. & Qiu, F. (2022). Microstructures, compressive residual stress, friction behavior, and wear mechanism of quenched and tempered shot peened medium carbon steel. *Wear*. 488, 204131. https://doi.org/10.1016/j.wear.2021.204131.
[16] Janka, L., Berger, L. M., Norpoth, J., Trache, R., Thiele, S., Tomastik, C., Matikainen, V. & Vuoristo, P. (2018). Improving the high temperature abrasion resistance of thermally sprayed Cr3C2-NiCr coatings by WC addition. *Surface and Coatings Technology*. 337, 296-305. https://doi.org/10.1016/j.surfcoat.2018.01.035.
[17] Wu, S., Wang, D., Tao, X., Wang, X., Zhang, R., Zhou, Z., Zhang, S., Wu, C., Sun, X., Zhou, Y. & Cui, C. (2024). Tempering temperature dependence on the microstructure, mechanical properties and wear behaviour of a novel high chromium cast iron. *Tribology International*. 197, 109831. https://doi.org/10.1016/j.triboint.2024.109831.
[18] Sarac, M.F. & Dikici, B. (2019). Effect of heat treatment on wear and corrosion behavior of high chromium white cast iron. *Materials Testing*. 61(7), 659-666. https://doi.org/10.3139/120.111382.
[19] Yu, Z., Li, L., Zhang, D., Shi, G., Yang, G., Xu, Z. & Zhang, Z. (2021). Study of cracking mechanism and wear resistance in laser cladding coating of Ni-based alloy. *Chinese Journal of Mechanical Engineering.* 34, 1-14. https://doi.org/10.1186/s10033-021-00599-8.
[20] Han, X., Zhang, Z., Wang, B., Thrush, S. J., Barber, G.C. & Qiu, F. (2022). Microstructures, compressive residual stress, friction behavior, and wear mechanism of quenched and tempered shot peened medium carbon steel. *Wear*. 488, 204131. https://doi.org/10.1016/j.wear.2021.204131.
[21] Liu, Q., Chen, C., Zhang, M. & Wang, S. (2019). Effect of different heat treatments on the microstructural evolution and mechanical properties of Ni-Cr-Si alloy fabricated by laser additive manufacturing. *Journal of Materials Engineering and Performance*. 28, 4543-4555. https://doi.org/10.1007/s11665-019-04239-0.
[22] Keskar, N., Krishna, K.M., Gupta, C., Singh, J.B. & Tewari, R. (2022). The effect of Cr content on the microstructural and textural evolution and the mechanical properties of Ni-Cr binary alloys. *Materials Today Communications*. 33, 104831. https://doi.org/10.1016/j.mtcomm.2022.104831.
[23] Pramod, T., Sampathkumaran, P., Anand Kumar, S., Seetharamu, S., Nataraj, J.R., Prasad, R.V.S. (2023). Investigation of residual stress and elastic parameters affected due to variations in manganese content and cast section size in wear resistant high chromium irons. In International Conference on Processing and Fabrication of Advanced Materials, 6-8 September 2023 (pp. 323-339). https://doi.org/10.1007/978-981-97-5967-5_26.
[24] Al-Rubaie, K. S. & Pohl, M. (2014). Heat treatment and two-body abrasion of Ni-Hard 4. W*ear.* 312(1-2), 21-28. https://doi.org/10.1016/j.wear.2014.01.013.
[25] Rizov, B.L. (2017). Some results from the investigation of effects of heat treatment on properties of ni-hard cast irons. *International Journal of Engineering Research and Development*. 13(2), 30-35. e-ISSN: 2278-067X.

[26] ASTM E 915. (1984). Standard Method for Verifying the Alignment of X-ray Diffraction Instrumentation for Residual Stress Measurement. Annual Book of ASTM Standards, 03.01, 809-812.
[27] Mashetty, S., Sampathkumaran, P., Deshpande, S., Sirsgi, S. & Rao, M.V. (2023). The erosion phenomena affecting residual stress in nickel chromium alloyed irons. *Journal of Southwest Jiaotong Universitry.* 58(2), 845-857. ISSN: 0258-2724.
[28] Lyu, Y.T., Ay, H., Huang, Y.C., Hung, T.P., Jang, K., Lee, R. T., Hong, Z.H. & Tseng, P.H. (2023). Prediction of surface residual stress in grinding process. *The International Journal of Advanced Manufacturing Technology*. 1-22. https://doi.org/10.21203/rs.3.rs-3047963/v1.
[29] Grum, J., Zerovmk, P. (1997). *Residual stresses in steels after heat treatments and grinding*. WIT Press. DOI: 10.2495/SURF970041.
[30] Xu, L., Wang, F., Li, M., Li, F., Wang, X., Jiang, T., ... & Wei, S. (2023). Fabrication and abrasive wear property of high chromium cast iron with high vanadium and high nitrogen content (HCCI-VN). *Wear*. 523, 204828. https://doi.org/10.1016/j.wear.2023.204828.
[31] Tabrett, C.P. & Sare, I.R. (1997). The effect of heat treatment on the abrasion resistance of alloy white irons. *Wear*. 203-204, 206-219. https://doi.org/10.1016/S0043-1648(96)07390-5.
[32] Pramod, T., Sampathkumaran, P., Seetharamu, S., Dube, N., Vergis, B.R., Kumar, R.K. & Ranganathaiah, C. (2022). Evaluation of corrosion rate and scratch resistance in chromium alloyed irons influenced by manganese addition and process parameters. In Recent Trends in Electrochemical Science and Technology: Proceedings of Papers Presented at NSEST-2020 and ECSIRM-2020 (pp. 53-66). Singapore: Springer Singapore. https://doi.org/10.1007/978-981-16-7554-6_4.
[33] Lindroos, M., Valtonen, K., Kemppainen, A., Laukkanen, A., Holmberg, K. & Kuokkala, V.T. (2015). Wear behavior and work hardening of high strength steels in high stress abrasion. *Wear*. 322-323, 32-40. https://doi.org/10.1016/j.wear.2014.10.018.
[34] Pei, W., Zhang, Y., Yang, S., Li, X., & Zhao, A. (2022). Study of work-hardening behavior of high manganese steel during compression. *Materials Research Express*. 9(6), 066503, 1-8. DOI: 10.1088/2053-1591/ac6da4.
[35] Sampathkumaran, P. & Seetharamu, S. (2005). Erosion and abrasion characteristics of high manganese chromium irons. *Wear*. 259(1-6), 70-77. https://doi.org/10.1016/j.wear.2005.03.001.
[36] Soriano, C., Leunda, J., Lambarri, J., Navas, V.G. & Sanz, C. (2011). Effect of laser surface hardening on the microstructure, hardness and residual stresses of austempered ductile iron grades. *Applied Surface Science*. 257(16), 7101-7106. https://doi.org/10.1016/j.apsusc.2011.03.059.
[37] Weidner, A., Tirschler, W. & Blochwitz, C. (2005). Overstraining effects on the crack-opening displacement of microstructurally short cracks. *Materials Science and Engineering*: A, 390(1-2), 414-422. https://doi.org/10.1016/j.msea.2004.08.013.
[38] Hutchings, I. & Shipway, P. (2017). *Tribology: friction and wear of engineering materials.* Butterworth-heinemann.
[39] Sue, J.A. & Troue, H.H. (1991). High temperature erosion behavior of titanium nitride and zirconium nitride coatings. *Surface and Coatings Technology*. 49(1-3), 31-39. https://doi.org/10.1016/0257-8972(91)90027-T.
[40] Sherman, A.J., Smith, G., Dean Baker, M.R., Richard Toth, M.R. (2001). Cermet tool and die materials from metal coated powders. In 25th Annual Conference on Composites, Advanced Ceramics, Materials, and Structures: A: Ceramic Engineering and Science Proceedings (pp. 95-102). Hoboken, NJ, USA: John Wiley & Sons, Inc.. https://doi.org/10.1002/9780470294680.ch11.
[41] Sahadevan, P., Pon Selvan, C., Lakshmikanthan, A., Bhaumik, A., Cuautle, A.F. (2024). Effect of printing process parameters on tensile strength and wear rate of 17-4PH Stainless Steel deposited using SLM process. *Frattura ed Integrità Strutturale*. 70, 157-176. https://doi.org/10.3221/IGF-ESIS.70.09.
[42] Hatti, G., Lakshmikanthan, A. & Naveen, G.J. (2023). Microstructure characterization, mechanical and wear behavior of silicon carbide and neem leaf powder reinforced AL7075 alloy hybrid MMC's. *Frattura Ed Integrità Strutturale*, 17(65). https://doi.org/10.3221/IGF-ESIS.65.07.
[43] Girish Prasad, M., Vijay Kumar, S. & Avinash, L (2024). Evaluation of microstructure and mechanical properties of Al6005 MMCs reinforced with B4C via stir casting route and optimisation through ANOVA DOE technique. *Advances in Materials and Processing Technologies*. 11(1), 175-195. https://doi.org/10.1080/2374068X.2024.2306036.